frontiers in Water

TYPE Original Research
PUBLISHED 24 June 2026
DOI 10.3389/frwa.2026.1844899

OPEN ACCESS

EDITED BY
Melida Gutierrez,
Missouri State University, United States

REVIEWED BY
Giuseppe Francesco Cesare Lama,
University of Naples Federico II, Italy
Li-Li Han,
Xiamen University, China

*CORRESPONDENCE
Ran Wei
ran.wei@iws.uni-stuttgart.de
Wolfgang Nowak
wolfgang.nowak@iws.uni-stuttgart.de

RECEIVED 01 April 2026
REVISED 04 May 2026
ACCEPTED 13 May 2026
PUBLISHED 24 June 2026

CITATION
Wei R, Le AV, Liu B, Azari M, Oladyshkin S, Kappler A and Nowak W (2026) Household sand filters for heavy metal removal exhibit limited nitrification and risk of nitrate contamination. *Front. Water* 8:1844899. doi: 10.3389/frwa.2026.1844899

Household sand filters for heavy metal removal exhibit limited nitrification and risk of nitrate contamination

Ran Wei[1]*, Anh Van Le[2], Binlong Liu[3], Mohammad Azari[4], Sergey Oladyshkin[1], Andreas Kappler[3,5] and Wolfgang Nowak[1]*

[1]Department of Stochastic Simulation and Safety Research for Hydrosystems, University of Stuttgart, Stuttgart, Germany, [2]Applied Geochemistry, Institute of Earth and Environmental Sciences, University of Freiburg, Freiburg, Germany, [3]Department of Geosciences, University of Tübingen, Tübingen, Germany, [4]Department of Water Quality Management, Karlsruhe Institute of Technology, Karlsruhe, Germany, [5]Cluster of Excellence (EXC 3121): TERRA—Terrestrial Geo-Biosphere Interactions in a Changing World, University of Tübingen, Tübingen, Germany

High ammonium concentrations in groundwater (GW) pose substantial challenges to existing GW treatment systems, especially simplified systems like household sand filters (HSFs), which are commonly used for heavy metal removal in developing countries. We aimed to answer how the complex interplay of physical and biochemical processes influences ammonium dynamics in HSFs, thus providing insights to optimize HSFs' future operation. We previously conducted a series of column experiments mimicking HSFs. These experiments revealed limited nitrification, thus fluctuating ammonium removal, highlighting the need to identify and better manage the controlling processes in HSFs. Thus, we established a one-dimensional advective-dispersive-reactive model conditioned on data from column experiments under laboratory and field conditions. The model accounts for temporal variations in nitrification reaction kinetics, transport processes, and a previously unconsidered nitrate leaching process. The modeled breakthrough curves captured the complex dynamics of ammonium, nitrite, and nitrate concentrations in laboratory and field column experiments. We showed that potential lags in the biochemical reactions caused by multi-factor induced inhibitions (e.g., heavy metals) lead to limited nitrification. This was supported by the strong hysteresis of the kinetic rates of nitrification in response to ammonium and nitrite concentrations. The parameterized leaching process leads to the verified nitrate contamination. Our scenario analysis further confirmed the limited nitrification efficiency at current setting suggesting modification is needed to eliminate the inhibition effects.

KEYWORDS
ammonium removal, column experiments, dual Michaelis-Menten kinetics, household sand filters, nitrate contamination, nitrification, reactive transport

1 Introduction

Elevated levels of ammonium (NH_4^+) and heavy metals like iron (Fe^{2+}) and arsenic (As^{3+}) in groundwater (GW) pose adverse effects on human health when groundwater

is used as the drinking water source. Household sand filters (HSFs), which receive GW mixed with atmospheric oxygen pumped into the top compartment (Le et al., 2022b), are widely used for contaminant removal (Vu and Wu, 2022) in developing countries where the feeding groundwater contamination level is high (Winkel et al., 2011; Truong et al., 2022). The performances of HSFs were evaluated by various of studies (Berg et al., 2006; Nitzsche et al., 2015; Le et al., 2022a,b, 2024). The removal percentage for the dissolved Fe^{2+} and As^{3+} by HSFs could reach 99% and 95%, respectively (Le et al., 2022b). The removal percentage for NH_4^+ varies depending on the filter materials (Martikainen et al., 2018) (as low as 12% with sand only materials Le et al., 2022b). Characterizing the processes that lead to the low removal is challenging. This is because the physical, chemical, and microbially facilitated processes in HSFs interact in complex and poorly understood ways, and together influence NH_4^+ concentration dynamics.

Process-based models simulating nitrification in column experiments could provide quantitative and mechanistic understandings of the complex processes within HSFs, thereby offering optimization strategies to improve the NH_4^+ removal efficiency. Although NH_4^+ is ubiquitously present in GW, only a few process-based modeling studies addressed nitrification processes in HSFs. Two studies (Piñón-Villarreal et al., 2013; Kruisdijk et al., 2024) applied one-dimensional reactive transport models to nitrogen species concentration data from column experiments. Piñón-Villarreal et al. (2013) did not parameterize the intermediate formation and consumption for nitrite (NO_2^-). Because ammonia-oxidizing bacteria (AOB) generate NO_2^- during ammonium oxidation whereas nitrite-oxidizing bacteria (NOB) consume NO_2^- during nitrite oxidation, and both groups compete for oxygen and space within biofilms, any imbalance between them can lead to transient NO_2^- accumulation. Such accumulation in drinking water can pose environmental and health risks, for example, formation of carcinogenic *N*-nitroso compounds (World Health Organization, 2016; Picetti et al., 2022). Kruisdijk et al. (2024) used an empirical rate law (Schwarzenbach et al., 2005) to approximate the kinetic reaction rates, thus did not fully present the enzyme-catalyzed mechanisms of the nitrification processes (Malone et al., 2006). Two relevant studies (Chen et al., 2021; Wu et al., 2022) employed the mechanistic Constructed Wetlands 2-D model (Langergraber and Šimůnek, 2005) to mimic the biochemical and transport processes in the intermittent sand filters. However, both studies primarily focused on evaluating the biofilm growth and treatment efficiency in the context of decentralized wastewater treatment systems, instead of treating groundwater intended for household consumption. Recent pore-scale biofilm models treat biofilms as fluid-filled micro-porous media, where internal diffusion, advection, and evolving permeability regulate substrate delivery to embedded microorganisms (Dawi et al., 2024). Within this framework, Fe^{3+}-oxide flocs accumulating around nitrifying biofilms may increase local mass-transfer resistance by restricting O_2 and NH_4^+ transport to active cells, consistent with groundwater-filter studies linking Fe^{3+} flocs to delayed NH_4^+ oxidation and suppressed (AOB) activity (Corbera–Rubio et al., 2024).

In the present study, we aim to (1) clarify the mechanisms driving NH_4^+ removal efficiency within HSFs, (2) identify key reactive bottlenecks in the nitrification process, (3) provide insights to optimize filter operational conditions, and (4) direct future experimental designs to untangle unresolved reactive processes. To address these goals and challenges, we establish a one-dimensional transient advection-dispersion-reaction model parameterized with dual Michaelis-Mention kinetic reactions (Liu, 2007) to represent possible substrate-limited biochemical steps of nitrification. It also considers transient reactive mechanisms influenced by the growth dynamics of the nitrification bacteria, the inhibition effects, and the leaching process of nitrate (NO_3^-) from the immobile phase of the HSFs. We calibrated the model against NH_4^+, NO_2^-, and NO_3^- concentration data from column experiments conducted by Le et al. (2024) mimicking the nitrification processes in HSFs. We also conducted scenario analysis with the parameterization to highlight the optimal operating conditions of HSFs. Overall, our experimental data-driven modeling approach can be used as an informative predictive tool for the future design and optimization of HSFs.

2 Materials and methods

Our overall workflow starts with conducting column experiments that mimic the processes of HSFs in order to collect experimental data. Then we set up process-based models, for which the collected data provides constraints for the model parameters. Once the model parameterizations are validated by the data, we use the model to conduct scenario analysis to investigate the optimal conditions for future operations and improvements. Figure 1 illustrates our overall workflow.

2.1 Experimental data acquisition

Two filtration column experiments were conducted by Le et al. (2024), one in laboratory and one in field settings. Both experiments were performed on columns packed with similar sand materials. The former was injected with artificial groundwater (GW), and the latter with natural groundwater (compositions of both lab and field settings are in Supplementary Table S1. The main difference was the aqueous As^{3+} concentrations (4.1×10^{-3} mmol/L in artificial GW and 1.3×10^{-6} mmol/L – 6.7×10^{-6} mmol/L in natural GW). Details of the field site and data acquisition are provided by Le et al. (2024).

2.2 Stoichiometry and kinetics of nitrification

Nitrification is described by the following two-stage stoichiometric equations:

$$NH_4^+ + 1.5O_2 \xrightarrow{\text{AOB}} NO_2^- + 2H^+ + H_2O \quad (1)$$

$$NO_2^- + 0.5O_2 \xrightarrow{\text{NOB}} NO_3^- \quad (2)$$

During the first stage, catalyzed by ammonia-oxidizing bacteria (AOB), NH_4^+ is oxidized to NO_2^- (ammonium oxidation). During the second stage carried out by nitrite-oxidizing bacteria (NOB),

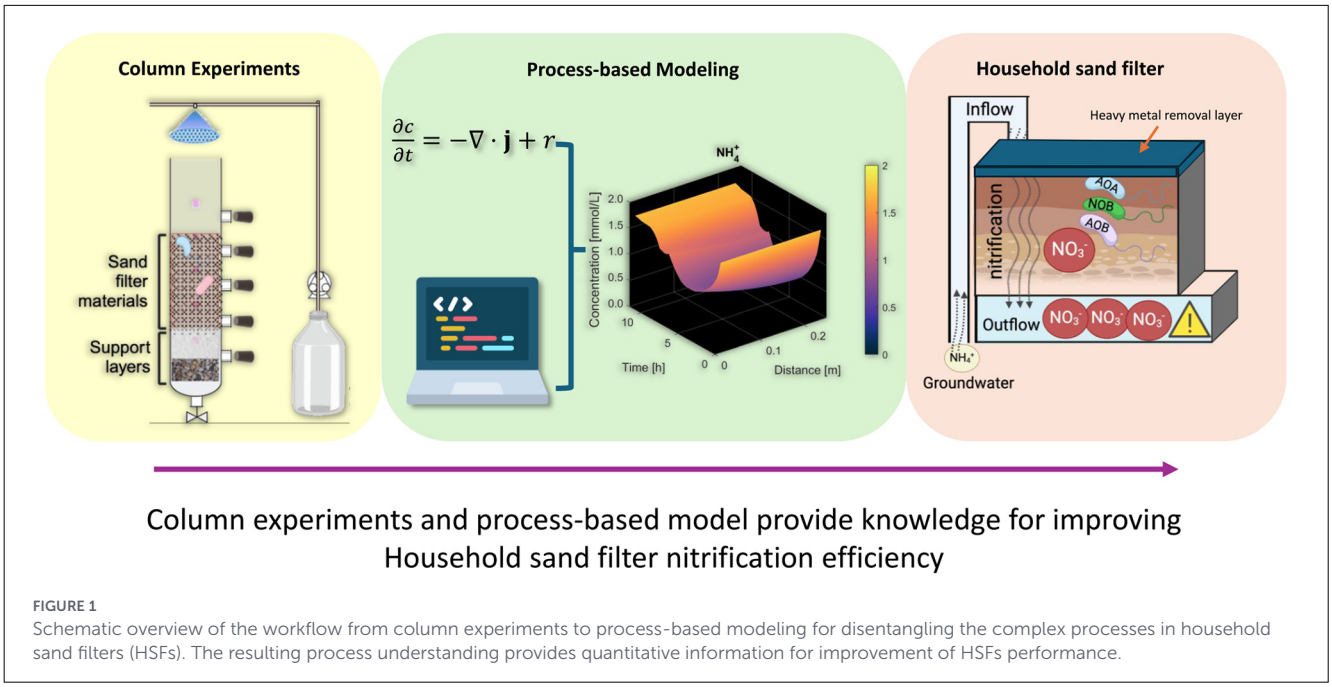

FIGURE 1
Schematic overview of the workflow from column experiments to process-based modeling for disentangling the complex processes in household sand filters (HSFs). The resulting process understanding provides quantitative information for improvement of HSFs performance.

nitrite is oxidized to nitrate (NO_3^-) (nitrite oxidation). Assuming that the concentrations of NH_4^+, O_2, and NO_2^- are limited, while the concentration of enzyme are sufficient (Malone et al., 2006), the kinetics for Equations 1, 2 are commonly parameterized using the dual Michaelis-Menten type of kinetics (Liu, 2007). Then, the rate [Mol/L^3/T] of ammonium oxidation (r_1) is expressed as:

$$r_1 = \mu_{\max 1} \frac{c_{NH_4^+}}{k_{m1,NH_4^+} + c_{NH_4^+}} \frac{c_{O_2}}{k_{m1,O_2} + c_{O_2}} \quad (3)$$

where $\mu_{\max 1}$ [Mol/L^3/T] ("Mol" represents amount of a substance; "L" represents length; "T" represents time) is the maximum rate coefficient; k_{m1,NH_4^+} and k_{m1,O_2} [Mol/L^3] are the half-velocity concentrations for NH_4^+ and O_2, respectively; $c_{NH_4^+}$ and c_{O_2} are the concentrations [Mol/L^3] of NH_4^+ and O_2, respectively. As $\mu_{\max 1}$ depends on the abundance of AOB that grows during the experiments, we model the $\mu_{\max 1}$ as a time-dependent variable and describe its temporal evolution using a logistic growth function:

$$\mu_{\max 1}(t) = \frac{k_{\max}}{1 + \exp[-r_{\max} \cdot (t - t_{\text{shift, max}})]} f_{\text{inhibition}} \quad (4)$$

where $k_{\max}$ [Mol/L^3/T] is the peak rate coefficient; $r_{\max}$ [1/T] is the steepness of $\mu_{\max 1}(t)$; $t_{\text{shift, max}}$ [T] is the time shift of the growth (a similar time-dependency was considered in Maggi and La Cecilia, 2016). An inhibition effect in ammonium oxidation was observed during the later stage of the field column experiment. Therefore, our Equation 4 contains a time-dependent inhibition factor [–]:

$$f_{\text{inhibition}} = \frac{1}{1 + \exp[r_{\text{inhib}} \cdot (t - t_{\text{shift\_inhib}})]} \quad (5)$$

where r_{inhib} [1/T] is the rate the maximum inhibition; $t_{\text{shift, inhib}}$ [T] is the delay of the inhibition effect. Equation 5 is an empirical representation of delayed loss of ammonium-oxidation capacity (inhibition) rather than a direct mass-balance description of heavy-metal accumulation. This delayed inhibition may reflect the progressive formation and deposition of inhibitory phases, for example, Fe^{3+}-oxide flocs and associated heavy-metal precipitates, on or near the filter media and nitrifying biofilms, which can reduce substrate transfer and/or suppress nitrifier activity over time.

The rate [Mol/L^3/T] of nitrite oxidation (r_2) is expressed as:

$$r_2 = \mu_{\max 2} \frac{c_{NO_2^-}}{k_{m2,NO_2^-} + c_{NO_2^-}} \frac{c_{O_2}}{k_{m2,O_2} + c_{O_2}} \quad (6)$$

where $\mu_{\max 2}$ [Mol/L^3/T] is the maximum rate coefficient; k_{m2,NO_2^-} and k_{m2,O_2} [Mol/L^3] are the half-velocity concentrations for NO_2^- and O_2, respectively; $c_{NO_2^-}$ [Mol/L^3] is the concentrations of NO_2^-.

2.3 Inter-phase mass-transfer of nitrate

We also considered the mass-transfer process of NO_3^- from the sand (immobile phase) to the water (mobile phase) during the filtration period, taking into account the transient influence of column clogging. The rate [Mol/L^3/T] of the transient inter-phase mass-transfer r_3 is parameterized by the linear-driving-force approximation (Sorwat et al., 2021):

$$r_3 = \frac{k_{\text{trans}}}{1 + \exp[-r_{\text{trans}} \cdot (t - t_{\text{shift, trans}})]} \cdot (c_{NO_3^-, \text{sand}} - c_{NO_3^-}) \quad (7)$$

where $c_{NO_3^-, \text{sand}}$ and $c_{NO_3^-}$ [Mol/L^3] are the NO_3^- concentration in the sand and water, respectively; k_{trans} [1/T] is the maximum transfer rate constant; r_{trans} [1/T] is the steepness of r_3; and $t_{\text{shift, trans}}$ [T] is the time shift of the mass-transfer.

2.4 Systems of advective-dispersive-reactive equations

The transport and reactive processes of the constituents in the columns are described by a system of 1-D advective-dispersive-reactive (ADR) equations. The rate of change of the concentration c_i [Mol/L^3] for the constituent i is expressed by Equations 8–12,

$$R_{NH_4^+}\frac{\partial c_{NH_4^+}}{\partial t} = -v_{\text{filt}}(t)\frac{\partial c_{NH_4^+}}{\partial x} + D(t)\frac{\partial^2 c_{NH_4^+}}{\partial x^2} - r_1 \quad (8)$$

$$R_{NO_2^-}\frac{\partial c_{NO_2^-}}{\partial t} = -v_{\text{filt}}(t)\frac{\partial c_{NO_2^-}}{\partial x} + D(t)\frac{\partial^2 c_{NO_2^-}}{\partial x^2} + r_1 - r_2 \quad (9)$$

$$\frac{\partial c_{NO_3^-}}{\partial t} = -v_{\text{filt}}(t)\frac{\partial c_{NO_3^-}}{\partial x} + D(t)\frac{\partial^2 c_{NO_3^-}}{\partial x^2} + r_2 + r_3 \quad (10)$$

$$\frac{\partial c_{O_2}}{\partial t} = -v_{\text{filt}}(t)\frac{\partial c_{O_2}}{\partial x} + D(t)\frac{\partial^2 c_{O_2}}{\partial x^2} - 1.5r_1 - 0.5r_2 \quad (11)$$

$$\frac{\partial c_{NO_3^-,\,\text{sand}}}{\partial t} = -\lambda_{\text{trans}} r_3 \quad (12)$$

where R_i [-] is the retardation factor for compound i (i: NH_4^+ Dou et al., 2016 and NO_2^- Piñón-Villarreal et al., 2013); v_{filt} [L/T] is the effective linear filtration velocity in the column; D [L^2/T] is the dispersion coefficient; r_i [Mol/L^3/T] is the net reaction rate for compound i; λ_{trans} [-] is the volume ratio of water and sand particles for the NO_3^- in the sand materials ($c_{NO_3^-,\,\text{sand}}$). We emphasize that since no measurement of the initial concentration $NO_{3,\text{sand}}^-$ was taken, it is treated as an estimated parameter. 1.5 [-] and 0.5 [-] are the stoichiometric coefficients in Equations 1, 2. The dispersion coefficient approximates the hydrodynamic dispersion according to the Scheidigger parameterization (Scheidegger, 1961; Strobel et al., 2023) (Equation 13):

$$D(t) = v_{\text{filt}}(t)\cdot\alpha + D_{\text{diff}}, \quad (13)$$

where α [L] is the dispersivity; D_{diff} [L^2/T] is the compound-specific pore-diffusion coefficient. Equations 8–11 were spatially discretized using finite differences (Noye and Tan, 1989) and, together with Equation 12, solved using the ordinary differential equation (ODE) solver *ode15s* (Shampine and Reichelt, 1997) in MATLAB.

We emphasize that, although heavy metal data were available (Le et al., 2024), the present dataset does not sufficiently constrain pathway-specific concentration-response relationships to justify explicitly coupling heavy metal dynamics to the nitrogen species. Instead, inhibition was represented parsimoniously by an effective time-dependent term.

2.5 Inflow boundary condition, effective filtration velocity, and initial condition

We applied fixed concentration (Dirichlet) boundary conditions (BC) of NH_4^+, NO_2^-, NO_3^-, and O_2 at the inlet and set gradient to zero at the outlet for solving Equations 8–11. During the experiments, multiple cycles of filtration were conducted over 2 months (waiting periods included). The effective filtration velocity, v_{filt} [L/T], is computed by dividing the column length L_{col} [L] by the filtration time [T]. The idealized filtration period was determined by removing the waiting periods from the experimental period. We assumed that the initial concentrations of NH_4^+, NO_2^-, NO_3^-, O_2, and NO_3^-, *sand* were uniform throughout the column, and treated them as estimated parameters.

2.6 Physical parameter inference and sensitivity

We calibrated the model using NH_4^+, NO_2^-, and NO_3^- concentration measurements taken at the field and lab column outlets (Le et al., 2024). The initial calibration ranges of all estimated parameters are in Supplementary Table S4 for the lab columns, and Supplementary Table S8 for the field columns. *lsqnonlin* algorithm (trust-region-reflective searching method Liu et al., 2020) in MATLAB was used to find the optimal parameter values by minimizing the objective function (Supplementary Equation S1). The normalized root-mean-square error (NRMSE Supplementary Equation S2) was computed to evaluate the goodness of the model fit. The remaining post-calibration uncertainty of the parameters was estimated by computing the covariance matrix (Supplementary Equations S3–S6). Finally, we identified the parameters to which the model output, in particular the modeled NH_4^+ concentration at the column outlet, is sensitive by computing SHapley Additive exPlanations (SHAP) values (Lundberg and Lee, 2017) (Supplementary Equation S7).

2.7 Scenario analysis

To evaluate the HSFs performance in ensuring regulatory compliance, with the calibrated model, we conducted a scenario analysis. We (1) simulated NH_4^+ concentration at the column outlet across various NH_4^+ inflow concentrations (15, 5, 2.5, and 1 [mmol/L]) using the minimum of the field column filtration velocity (Supplementary Figure S12D, thus the longest contact time), comparing the results with and without inhibition to the target NH_4^+ concentration (2.77×10^{-2} [mmol/L] specified by the European Union (EU) Directive on water quality (European Union, 2020). We (2) compared the contact time needed to reach the same target NH_4^+ concentration under different inflow concentrations (15, 5, 2.5, and 1 [mmol/L]) using the mean field column filtration velocity.

The remainder of the article is organized as follows: first, we summarize the model's performance and discuss the processes driving the dynamics of the constituents in the column experiments. Second, we analyze and interpret the relationships between the reaction rates and the concentrations of nitrogen species. Third, we show the scenario analysis results for optimally operating the household sand filters. Additionally, we compare other models with our model and justify our approach. Lastly, we propose future experiments to disentangle the complex inhibition effects.

3 Results and discussion

3.1 Overall model performance on *N*-species and O_2

Since the columns were fed from the top and effluent was collected from the bottom, a plug flow regime was established, resulting in a heterogeneous (bio)filtration environment. The current design of HSF systems, therefore, experiences fluctuations in the measured effluent concentrations of NH_4^+, NO_2^-, and NO_3^-. Figure 2 shows the breakthrough curves (BTCs) of the five constituents at the outlet of the column in laboratory (lab column) and field settings (field column). The inflow boundary conditions were processed as stepwise time-series signals. Supplementary Figure S1 shows the inflow concentrations and the effective filtration velocity for the lab column, while Supplementary Figures S12, S13 show that of the field column 1 and 2.

For the lab column, the modeled NH_4^+ and NO_3^- concentrations yielded the NRMSE value (Supplementary Equation S2) of 14.8% and 24.1%, respectively, while NO_2^- concentrations stayed below detection limit. For the field column, the modeled NH_4^+, NO_2^-, and NO_3^- concentrations yielded the NRMSE value of 39.9%, 37.3%, and 28.4%, respectively. The modeled space-time distributions of lab columns concentrations of NH_4^+, NO_2^-, NO_3^-, O_2, and $NO_{3,\,\text{sand}}^-$ are shown in Supplementary Figures S2, S3, while those for the field columns are shown in Supplementary Figures S14, S15.

3.2 Temporal dynamics of the constituents in the lab column

The lab column exhibited limited NH_4^+ removal efficiency. At the end of the 20-h idealized filtration period (see Subsection 2.5 inflow BC and filtration velocity), 24.39% ($1 - \frac{\int c_{\text{outlet}} \cdot V\, dt}{\int c_{\text{inlet}} \cdot V\, dt}$; c_{inlet} and c_{outlet} are the concentrations at the inlet and outlet of the column, respectively.) of the inflow NH_4^+ was removed at the outlet. Figure 2A shows that NH_4^+ at the column outlet remained almost constant throughout the idealized filtration period, particularly during the first seven hours. The low NH_4^+ consumption rate was attributed to the lag phase of ammonium oxidizing bacteria (AOB) within the column before initiating the NH_4^+ oxidation (see our time-dependent maximum logistic growth rate $\mu_{max1}(t)$ (Equation 4). An exception was at approximately the sixth hour when NH_4^+ concentration was reduced due to a drop of the filtration velocity at the same time (Supplementary Figure S1C). The velocity drop resulted in an extended contact time for the solute within the column, allowing for longer progress of the kinetic reactions before the constituents were transported out of the column. A similar trend was observed between the 11th and 18th hour where NH_4^+ oxidation became more pronounced as the solute velocity winded down (Supplementary Figure S1C).

The NO_3^- concentration in the lab column showed large increases during the first eighth hours of idealized filtration period, peaked at the fifth hour then started receding after 8 h (Figure 2C). In contrast, during the same period, NH_4^+ concentration stayed almost constant (Figure 2A), indicating that the large increase of NO_3^- concentration was not mainly caused by the microbial-facilitated nitrification process. This implication is further supported by the fact that during the later stage (10–15th hour), NH_4^+ concentration experienced a slight declining period, whilst NO_3^- correspondingly showed the second but more dispersed period of increase. Therefore, the early large increase of NO_3^- was caused by process(es) that had not been previously considered. NO_3^- leaching out from the sand materials into the water phase in soil column experiments was reported in various literature (Das et al., 2023; Dai et al., 2023), which was the most plausible process in our experiments that led to the large increase of NO_3^-. The parameterization of delayed NO_3^- mass transfer driven by the concentration gradient between the sand and water phases (Piñón-Villarreal et al., 2013) considered the influence of column clogging which caused by precipitation of heavy metal oxides and carbonates minerals (Le et al., 2024). The parameterized time-dependent first-order mass-transfer process (Equation 7) led to the good agreement of the modeled NO_3^- BTC with the measurement in the water phase. The modeled NO_2^- concentration was at extremely low level (maximum 7.14×10^{-8} [mmol/L], below the detection limit) (Figure 2B), indicating high nitrite oxidation rate compared to ammonium removal activity. Similar findings were reported in Tatari et al. (2016). The modeled O_2 (Figure 2D) showed rapid depletion, which also contributed to the incomplete NH_4^+ removal. Overall, the combination of insufficient O_2 and low amount of active AOB led to the incomplete ammonium oxidation process in the lab column.

3.3 Temporal dynamics of the constituents in the field column

The field column exhibited higher ammonium removal efficiency than the lab column. Over the 11.5-h idealized filtration period, 53.69% of the inflow NH_4^+ was removed at the outlet. Figure 2F shows that NH_4^+ concentration at the column outlet experienced a prolonged drop over the course of the first seven hours. Afterwards, the concentration nearly returned to the inflow concentration level (1.5 [mmol/L]). This higher NH_4^+ elimination at early time, compared to the lab column, indicates a more active AOB community already present in the field column, whereas AOB in the lab column needed more time to grow. The re-bounce of NH_4^+ concentration at 8th-hour and later could be described by the delayed inhibition effect at the first stage of the ammonium oxidation in Equation 4. The delay of the inhibition effect was captured by the time-dependent inhibition factor in Equation 4. Heavy metals such as iron (Fe) and arsenic (As) were reported inhibiting NH_4^+ oxidation (Qu et al., 2022; Corbera–Rubio et al., 2024). Corbera–Rubio et al. (2024) reported that Fe^{3+} flocs produced during the Fe^{2+} oxidation inhibits ammonium oxidation by limiting the activity of AOB. In our lab experiments, the injected groundwater also contained dissolved Fe^{2+} (2.3×10^{-1} [mmol/L]), As^{3+} (1.3×10^{-6} [mmol/L]), and Mn^{2+} (3.3×10^{-2} [mmol/L]). The specific reason causing the delay of inhibition of the ammonium oxidation is not clear since the mechanism of Fe^{3+} flocs inhibition on AOB oxidizing capacity is unknown (Corbera–Rubio et al., 2024). Comparing the lab and

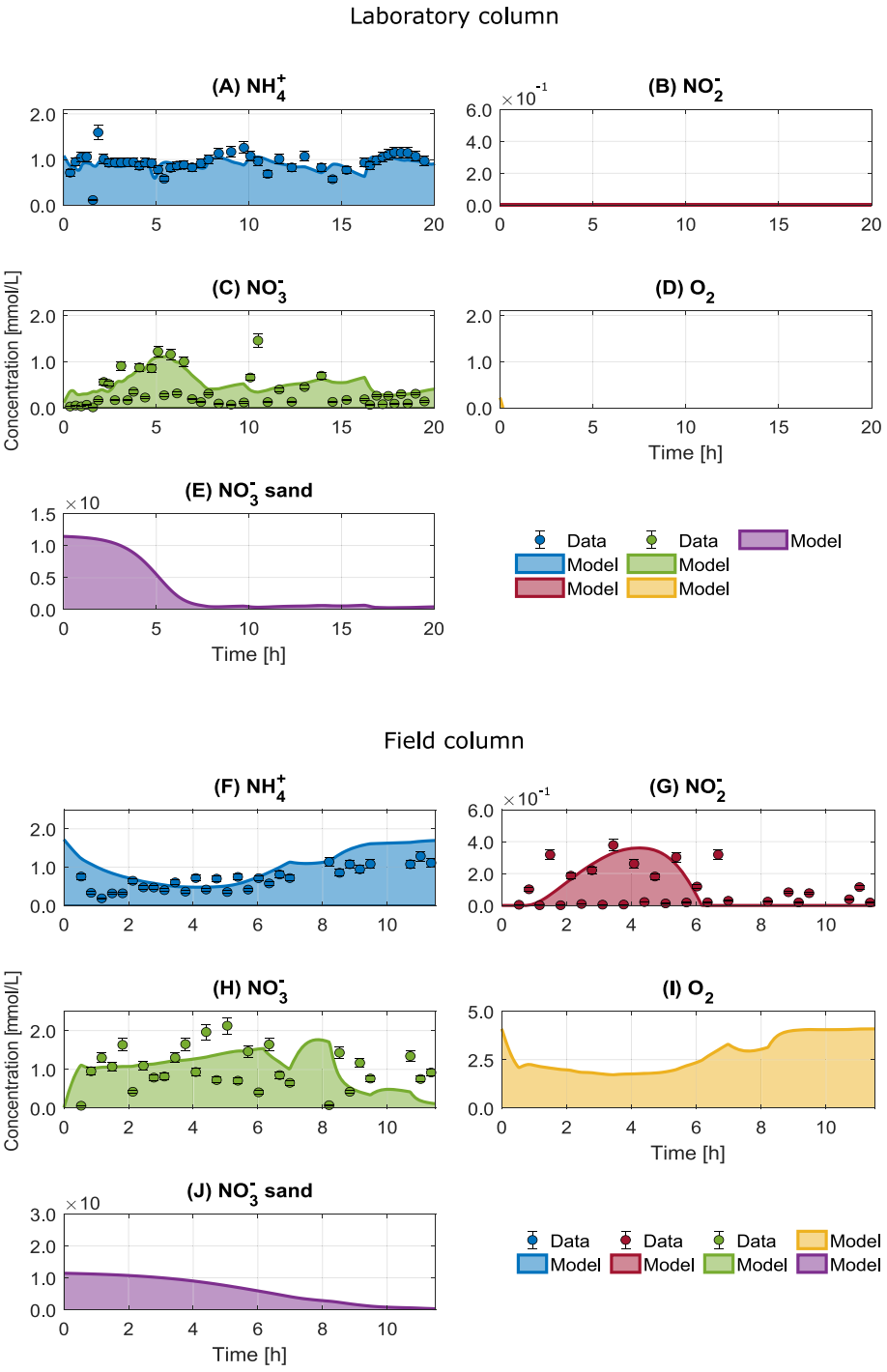

FIGURE 2
Breakthrough curves at the outlet of the lab **(A–E)** and field **(F–J)** columns for the five species. The simulated NO_2^- concentration in the lab column **(B)** is on the order of magnitude of 10^{-8} [mmol/L], thus it is no plotted. A 10% error is assumed for all measurements.

field columns, the fitted k_{max} for NH_4^+ oxidation in the lab column is one order of magnitude lower than that of the field column (equivalent to 10 times lower inhibition factor, $f_{\text{inhibtion factor}}$), due to the much higher As^{3+} concentration (4.1×10^{-3} mmol/L) (Papirio et al., 2014; Qu et al., 2022) (Supplementary Table S1).

Limited biological abundance might also lead to the lower $k_{\max}$in the laboratory column. However, this explanation is not well-supported under our experimental conditions as direct measurements of initial microbial abundance, for example, cell counts or *amoA* gene copy numbers, were not available. The laboratory columns were not initiated with sterile or biomass-free material, as the reactive layer was prepared from sand collected from actively used household filters, although sampling, cold storage, homogenization, and repacking may have disrupted

established biofilms and temporarily reduced microbial activity. In contrast, the field columns were packed with commercially sourced pre-cleaned sand, but the repeated addition of natural groundwater during the experiment may have supplied active microorganisms and supported microbial reactivation. Therefore, true *de novo* biofilm formation in the laboratory columns is unlikely, and Equation 4 should not be interpreted as assuming zero initial biomass; rather, differences in acclimation or reactivation are implicitly reflected in $t_{shift,max}$. While some contribution from differences in initial microbial activity cannot be excluded, the lower k_{max} in the lab setting (0.2 s^{-1}) than the field setting (0.55–1.8 s^{-1}) despite the likely presence of attached biomass supports As^{3+} inhibition as an important controlling factor, although not necessarily the sole factor.

NO_3^- concentration in the field column (Figure 2H) shows the corresponding dynamics to those of NH_4^+, experiencing the prolonged increase during the same period when NH_4^+ was largely consumed. However, based on the stoichiometry (Equations 1, 2), the bioreaction alone was not sufficient to produce the observed NO_3^- concentration level since 53.69% of NH_4^+ with constant inflow concentration of 2 [mmol/L] (Supplementary Figure S13A) was removed, but NO_3^- concentration was oscillating around 1.7 [mmol/L]. Moreover, the NO_2^- concentration (Figure 2G) showed a pronounced peak that was captured by the modeled BTC, whereas NO_2^- was fully consumed in the lab column. This suggests a high AOB activity, but a low activity in nitrite oxidation bacteria (NOB), especially considering that the O_2 concentration was sufficient and matched the NH_4^+ dynamics (Figure 2F). Similar to the lab column, only with the inclusion of a transient first-order mass-transfer process characterizing the leaching of NO_3^-, then the modeled BTCs could effectively describe the measured NO_3^- dynamics.

In real-world household operation, the NO_3^- leaching effect may be periodically enhanced by intermittent use or backwashing. Although direct evidence for backwashing-induced NO_3^- leaching in household sand filters is limited, studies on analogous drinking-water biofilters and rapid sand filters show that backwashing can influence NH_4^+ removal, particularly nitrification, by disturbing filter media, removing accumulated flocs or excess biofilm, and altering substrate transfer to nitrifiers (Laurent et al., 2003; Niu et al., 2018; Boersma et al., 2025). Therefore, disturbance of nitrate-containing sand/filter materials during backwashing or flow restart may plausibly increase NO_3^- release, producing a transient effluent pulse. Since this mechanism was not explicitly tested here, future studies should monitor nitrogen species immediately before and after backwashing.

3.4 Reactive rates on *N*-species concentrations

The relationships of reactive rates and their corresponding nitrogen species concentrations shared insights of the underlying mechanism of incomplete nitrification. Figure 3 illustrates the reactive rates (Equations 3–6) and the modeled nitrogen species concentrations over time at different locations in both lab and field columns. For the lab column, Figures 3A–C (observed the narrow range on the *x*-axis) show that the ammonium oxidation rate remained nearly constant over time under different NH_4^+ concentrations. This suggests that the rate of ammonium oxidation quickly reached steady, possible near-equilibrium conditions, throughout the column. The lack of spatial and temporal variability in the relationship of NH_4^+ oxidation rates and concentrations means that the ammonium oxidation rate was likely repressed, caused by the inhibition from heavy metals like As^{3+}. NO_3^- shows (Figures 3D–F) a strong counter-clock-wise hysteresis, in which the production rates are higher than the NH_4^+ oxidation rate, indicating an external source term for NO_3^-. The hysteresis is caused firstly by the time shift dominant leaching process (red arrow; Equation 7). Afterwards the rate decreased due to the reduced concentration gradient (black arrow). Similar hysteresis patterns have also been observed in other reactive systems (Störiko et al., 2021, 2022; Di Curzio et al., 2024).

For the field column, Figure 3 shows that during both stages of nitrification, the nitrogen species concentrations and their production rates experienced hysteresis. In particular, the NH_4^+ concentration and its consumption rate (Figures 3G–I) experienced a stronger non-linear pattern than that in the lab column. An initially higher (than the lab column) ammonium oxidation rate was observed throughout the column. The clock-wise hysteresis indicated the high AOB activity in the field column, and its activity was inhibited at later time by heavy metal (lower As^{3+} concentration in natural GW) as the NH_4^+ started to accumulate (purple arrow). This delayed inhibition occurred throughout the column. Figures 3J–L illustrate that the production rates of NO_3^- and its concentration experienced stronger (counter-clock-wise) hysteresis than that in the lab column. The hysteresis is at first caused by the nitrite oxidation (blue arrow; Equation 2), followed by the combination of enhanced nitrite oxidation (increased NOB activity) and the time shift dominant leaching process (yellow arrow). Next, the hysteresis loop shows nitrite oxidation and leaching with reduced NO_3^- concentration gradient (brown arrow). Lastly, the sudden increase in the middle of the hysteresis loop was caused by the clogging (velocity drop at the sixth-hour of the idealized filtration time in Supplementary Figure S12) that later on transitioned to an inhibition period (green arrow).

For both columns, when moving from the inlet to the outlet, the hysteresis became more pronounced and the loops widened. This was caused by increasing spatial heterogeneity (e.g., different sections of the column experienced varying levels microbial activities) within the system, indicating that as NH_4^+ decreased and NO_3^- accumulated toward the outlet, the system experienced diffusion and advection effects, where NO_3^- was spread more unevenly across the column. Therefore, spatial heterogeneity in the reaction environment, combined with complex transport and reaction dynamics, simultaneously affects the nitrification process. The widening of the hysteresis loops should not be interpreted as a stronger deviation from the steady-state from the inlet to the outlet, because the temporal forcing (microbial activity, inhibition, and nitrate leaching) that drives transient behavior acts throughout the column rather than increasing monotonically downstream. Thus, the wider downstream hysteresis loops reflect enhanced transport-reaction coupling and system memory along the column. The modeled space-time distributions reaction rates are shown in Supplementary Figures S6,

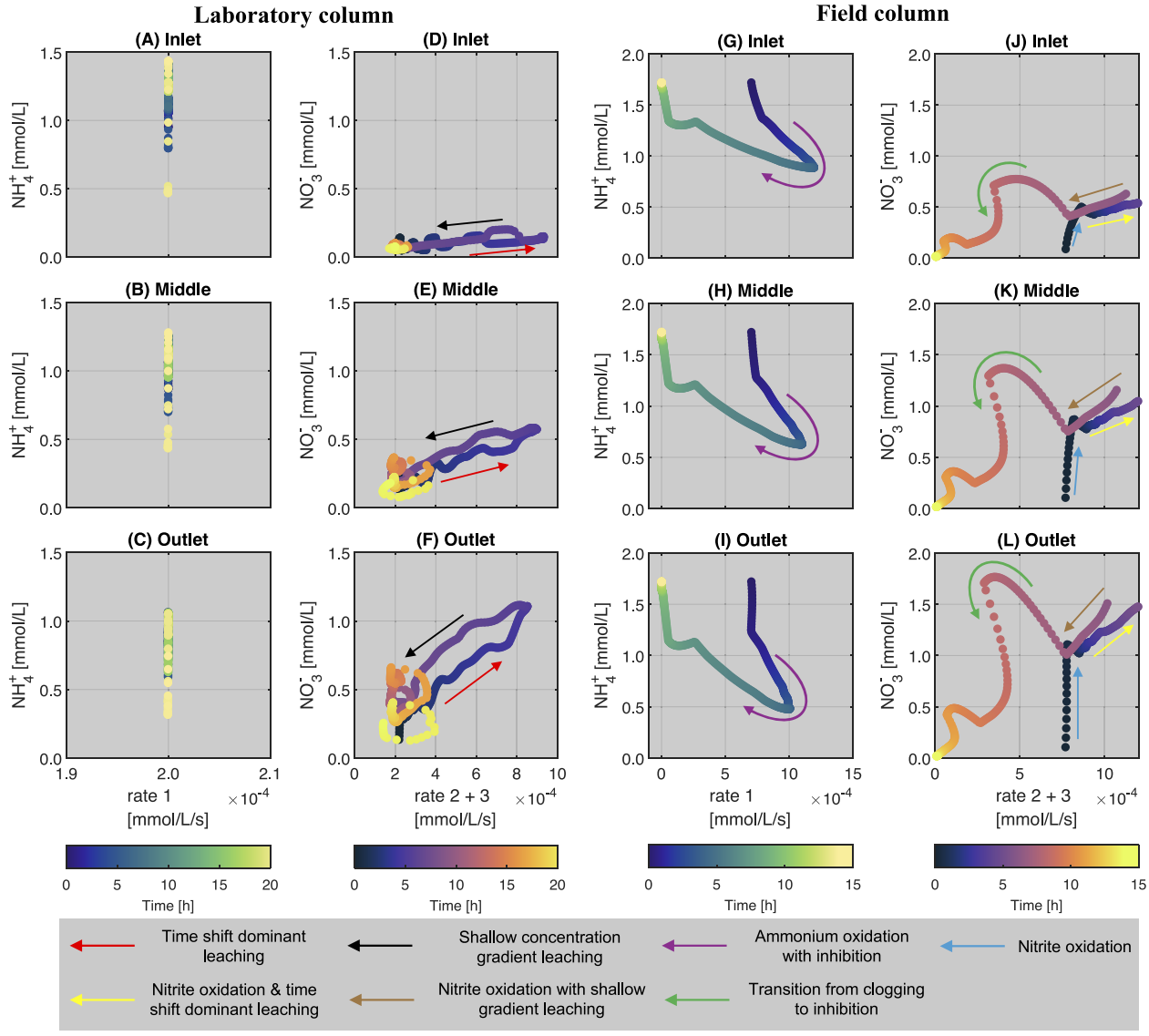

FIGURE 3
Relationships between the reactive rates (Equations 3–7) and NH_4^+ and NO_3^- concentrations in lab **(A–F)** and field columns **(G–L)**. Subplots on each row show the relationship over time at the inlet, middle, and outlet of the same column.

S7 for the lab columns, and Supplementary Figures S20, S21 for the field columns. The estimated parameter values for laboratory columns are in Supplementary Tables S2, S3, and their distributions in Supplementary Figures S8, S9, while those for the field columns are shown in Supplementary Tables S6, S7 and Supplementary Figures S16, S17, respectively.

3.5 Scenario analysis: required filtration velocity and contact time

NH_4^+ removal is heavily dependent on the contact time in the column. Figures 4A, B show the modeled BTCs of NH_4^+ concentrations at the field column outlet, under constant injection of different NH_4^+ inflow concentrations. Under the current bioreactive parameter settings, with sufficient oxygen supply and no inhibition effects within the field column (Figure 4A), only the lowest concentration of injected NH_4^+ [1 mmol/L] could be reduced to the drinking water standard of 2.77×10^{-2} [mmol/L] (European Union, 2020) after 1.3 h of idealized filtration time (mean field column velocity 2.0×10^{-4} [m/s]). When inhibition was included, NH_4^+ could still be reduced to the target concentration with the same filtration velocity for inflow NH_4^+ of 1 mmol/L. However, the delayed inhibition (e.g., heavy metal flocs) leads to rebound of NH_4^+ concentration (purple line). The removal percentage became limited when the inflow concentration was extremely high (e.g., 15 [mmol/L] in Figure 4B). Figure 4C shows the contact time needed to reach the target concentration when the mean field experimental velocity (Supplementary Figure S13D) was used as the effective filtration velocity in the model. The required contact time increased with the higher inflow NH_4^+

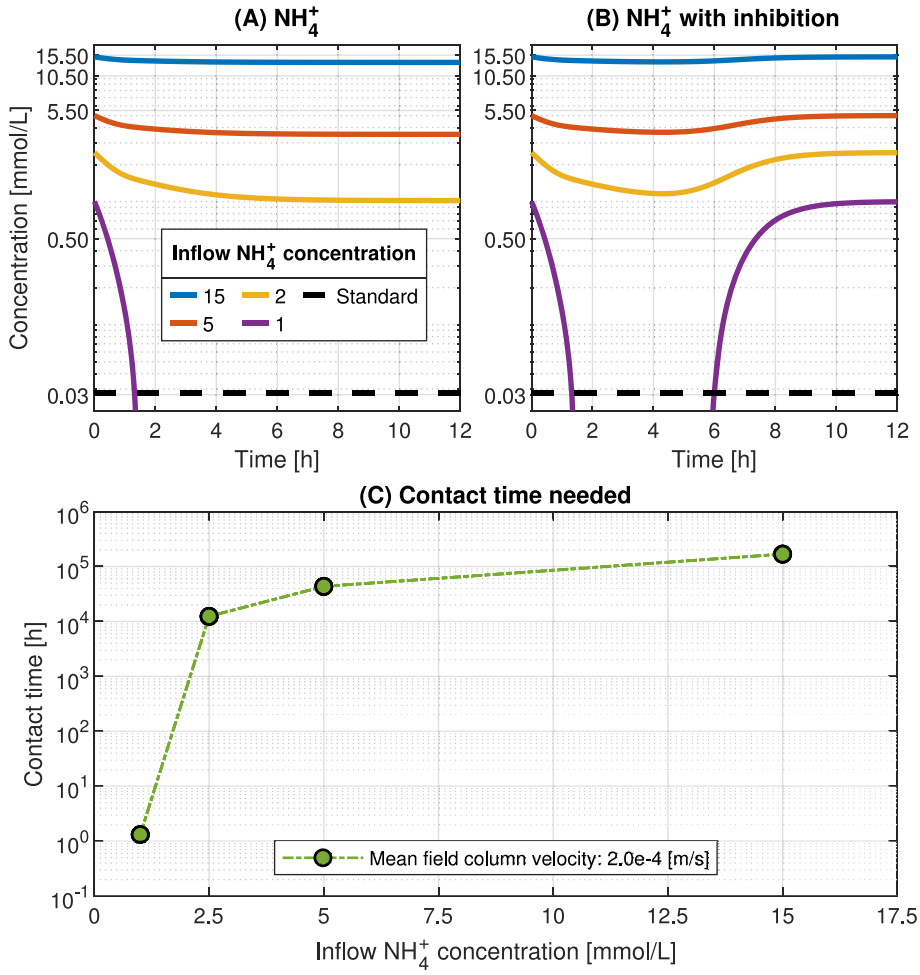

FIGURE 4
The simulated breakthrough curves of NH_4^+ concentrations at column outlet under different inflow NH_4^+ concentrations with calibrated reaction parameters obtained from field experiment settings. **(A)** does not include inhibition, whereas **(B)** includes inhibition. Standard represents the target NH_4^+ concentration specified by European Union Directive on water quality (European Union, 2020). **(C)** shows the contact time needed to reach the target NH_4^+ concentration, with various inflow NH_4^+ concentrations. Simulations in **(A, B)** were conducted using the minimum of the field column filtration velocity. Simulation in **(C)** was conducted using the field column parameter sets without inhibition effects, under mean field column filtration velocity.

concentrations. The required contact time increased by four orders of magnitude (high as 1.68×10^5 h for 15 mmol/L of inflow NH_4^+), which is impractical for real-world household applications. Thus, the transport process played a significant role in the current bioreactive environment, however, further investigation is needed to investigate the cause of the inhibition effect and its mitigation methods. The SHAP values of the parameters with respect to the nitrogen and oxygen concentrations in lab columns and field columns are shown in Supplementary Figures S10, S11, S18, S19, respectively.

3.6 Comparison with existing modeling approaches

As mentioned in the introduction, two previous studies (Piñón-Villarreal et al., 2013; Kruisdijk et al., 2024) have addressed 1-D reactive transport models for household sand filters (HSFs); however, these models lacked a full representation of nitrogen species dynamics and did not explicitly consider the biological enzymatic reactions governing nitrification. Two other studies (Chen et al., 2021; Wu et al., 2022) applied the Constructed Wetland 2-D model (CW2D) coupled with HYDRUS. CW2D was specifically designed for constructed wetlands technologies, and originally developed by Langergraber and Šimůnek (2005) based on the Activated Sludge Model No. 1 (ASM1) which is recommended by International Water Association (IWA) (Henze et al., 2006) for wastewater treatment, not modeling drinking water treatment systems such as HSFs.

Moreover, these CW2D-based models used default stoichiometric and calibrated kinetic parameters for municipal wastewater treatment scenarios, where influent concentrations of organic carbon and concentration of nitrifying bacteria are significantly higher than in household sand filters (HSFs) designed for drinking water treatment. In HSFs, the influent typically contains very low biomass concentrations, making the microbial colonization and biofilm development within the sand matrix a

more critical determinant of treatment efficiency. Additionally, the hydraulic retention time (HRT) and filtration rates in drinking water HSF systems are shorter and higher, respectively, compared to sand filters used for wastewater treatment. This is because drinking water applications demand higher throughput with stringent effluent quality, whereas wastewater sand filters operate under lower filtration rates to maximize substrate contact and reaction times. Such fundamental differences in loading regimes directly influence substrate-biomass interactions, biofilm development patterns, and the kinetics of ammonium oxidation and nitrate removal. Additionally, nitrate leaching dynamics from the solid phase to the mobile water phase, which are critical in determining effluent nitrate levels in drinking water HSFs, are not considered in the CW2D module. As a result, such CW2D-HYDRUS cannot well-simulate leaching concentration of nitrate from the sand matrix. So we believe these CW2D-based models are not appropriate for HSFs.

Our model incorporates advection-dispersion-reaction processes and is parameterized with dual Michaelis-Menten kinetics with time-dependent parameters to capture the transient enzymatic dynamics of nitrification in HSFs under varying operational conditions. The model captures spatiotemporal variations in all nitrogen speciations, accounts for substrate diffusion limitations, inhibition factors, and leaching of nitrate from the immobile phase.

3.7 Future experiments for differentiating the possible heavy metal inhibition pathways

The current modeling results indicate that heavy metals inhibit nitrification. However, the available data, including the heavy metals (Le et al., 2024), are insufficient to explicitly explain the inhibition mechanisms. Targeted experiments are needed before increasing model complexity further. The contrasting behavior of the laboratory and field columns suggests that the fitted inhibition factor (Equation 5) likely represents several non-exclusive heavy-metal inhibition pathways rather than a single, generic process. In the laboratory column, the higher As^{3+} concentration in the artificial groundwater than that of the natural groundwater coincided with persistently limited NH_4^+ removal, negligible modeled NO_2^-, and rapid O_2 depletion, which is consistent with strong suppression of ammonia oxidation. However, the rapid O_2 depletion is not uniquely diagnostic of direct *As* toxicity, and may also reflect oxygen consumption during Fe^{2+} oxidation. In the field column, NH_4^+ first decreased and then rebounded after about 7–8 h, while NO_2^- showed a pronounced transient peak despite sufficient O_2. This indicates delayed inhibition and a possible imbalance between ammonia oxidation and nitrite oxidation. Together, these results support three plausible pathways: direct *As* toxicity to microorganisms, including nitrifiers (Papirio et al., 2014; Qu et al., 2022), *Fe*-mediated inhibition associated with Fe^{3+} flocs formed during Fe^{2+} oxidation suppressing the nitrification (Corbera–Rubio et al., 2024), and a possible stronger inhibition of NOB than AOB, as suggested by the transient NO_2^- peak observed in the field column. Figure 5A shows the possible mechanistic pathways of heavy metal inhibition, where the hypothesized causality is summarized from upstream chemical drivers to mechanistic pathways, immediate biological effects, and representative fingerprints (i.e., the specific measurable experimental patterns expected for each mechanism).

To differentiate these pathways, the experiments should aim to diagnose the fingerprints summarized in Figure 5B. A first step should therefore be short-term batch assays (Corbera–Rubio et al., 2024) using active filter material or detached biomass under separate treatments: As^{3+}, As^{5+}, dissolved Fe^{2+} under oxic conditions, preformed Fe^{3+} flocs, and floc-free supernatant after *Fe* oxidation. The main measured outputs should include concentrations of NH_4^+, NO_2^-, NO_3^-, dissolved O_2, *Fe* and *As* speciation, and, if feasible, intracellular metal accumulation and transcriptional responses of nitrification functional genes, including the ammonia monooxygenase subunit A gene (*amoA*), hydroxylamine oxidoreductase gene (*hao*), and nitrite oxidoreductase subunit A and B genes (*nxrA*/*nxrB*). As shown in Figure 5B, stronger inhibition by As^{3+} than by As^{5+}, together with intracellular metal accumulation and reduced *amoA*/*hao* expression, would be most consistent with direct *As* toxicity. In contrast, stronger inhibition by preformed Fe^{3+} flocs than by dissolved Fe^{2+}, particularly if nitrification activity recovers after washing or backwashing, would be most consistent with *Fe*-mediated inhibition. Likewise, NO_2^- accumulation together with a stronger response of *nxrA*/*nxrB* than *amoA*/*hao* would most strongly support NOB-selective inhibition. Such experiments should ideally combine nitrification rate measurements with molecular targets, because nitrification rates and functional genes such as *amoA* and *nxrA* can respond differently under contaminant stress, and heavy-metal exposure can differentially affect nitrifying functional groups (Hou et al., 2023).

A second step should be a depth-resolved column experiment designed to test whether the spatial fingerprints proposed in Figure 5 emerge along the filter bed. This experiment should include sampling ports, DO/pH microprofiles, *Fe* and *As* speciation, and destructive sampling of deposits (e.g., Fe^{3+} flocs) along the column. In particular, a rapid recovery of NH_4^+ oxidation after washing, backwashing, or upstream removal of freshly formed flocs would support the reversible *Fe*-floc pathway reported by Corbera–Rubio et al. (2024). By contrast, inhibition linked mainly to As^{3+} exposure and intracellular accumulation would point to direct toxic stress. More generally, matching the observed response pattern to the fingerprints summarized in Figure 5B would allow the current lumped inhibition factor to be replaced in future models by mechanism-specific terms and would provide a direct experimental diagnosis of the conceptual pathways proposed in Figure 5A.

4 Environmental implications and future work

Household sand filters demonstrated limited efficiency in removing NH_4^+ from the inflow groundwater due to factors such

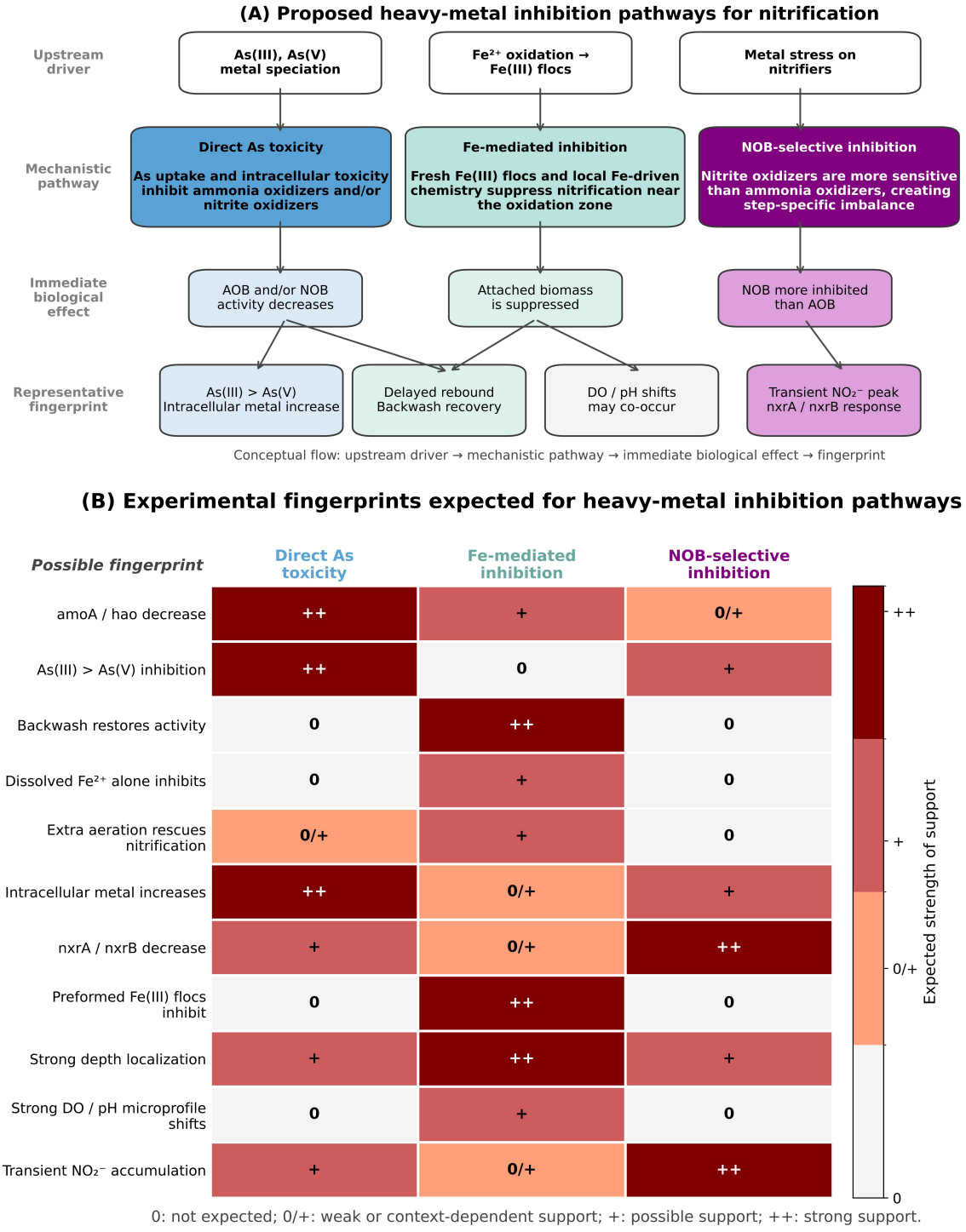

FIGURE 5
(A) Possible mechanistic pathways linking upstream chemical drivers to mechanistic pathways, immediate biological effects, and representative fingerprints. **(B)** The possible fingerprints are organized as a diagnostic matrix, showing how strongly each measurement supports each candidate inhibition pathway, thereby highlighting the most informative future experiments.

as the presence of high concentrations of heavy metals (e.g., As^{3+}) that suppress the activity of nitrifying microorganisms. The present study quantitatively highlights the processes in HSFs for NH_4^+ removal from GW, detailing for the first time the transient transport and kinetic reactive processes, including time-dependent inhibition effects and the previously unconsidered NO_3^- leaching process. The external source parameterized in our model suggests that the possible filter sand or filter material contained releasable nitrate, which coincides with the known NO_3^- contamination in soil from the agricultural area of the Red River delta (Smith et al., 2024). However, direct measurements of nitrate in the filter material would be needed to confirm this mechanism. Our scenario

analysis demonstrates that with the current transport and reactive parameter settings, sufficient NH_4^+ removal could be achieved within a reasonable time-frame (1.3 h for 1 mmol/L). However, the inhibition effect from, for example, heavy metals, must be eliminated to avoid the rebound of concentration, and enhanced removal methods are needed to reach the legal limit for NH_4^+ at high inflow concentration.

To address these challenges, we propose integrating a heavy metal removal mechanism within HSFs before the nitrification process. Adding a cost-effective activated carbon layer on top of the sand materials in HSFs could enhance the adsorption of heavy metals (Yang et al., 2019; Gilani and Prajapati, 2024) while preventing the clogging caused accumulation of the heavy metal flocs. The NO_3^- concentration at the column outlets is reaching the legal limit (8.06×10^{-1} mmol/L) (European Union, 2020). Therefore, routine monitoring of NO_3^- concentration levels in filtered water, particularly before and after backwashing, is essential to ensure continued safety.

Data availability statement

The original contributions presented in the study are included in the article/Supplementary material, further inquiries can be directed to the corresponding author/s.

Author contributions

RW: Writing – original draft, Software, Formal analysis, Writing – review & editing, Methodology, Visualization, Investigation, Data curation, Validation, Conceptualization. AL: Visualization, Formal analysis, Methodology, Conceptualization, Data curation, Writing – original draft, Resources, Writing – review & editing, Investigation. BL: Formal analysis, Writing – original draft, Software, Data curation, Visualization, Conceptualization, Methodology, Writing – review & editing, Investigation, Validation. MA: Visualization, Validation, Investigation, Formal analysis, Methodology, Writing – original draft, Writing – review & editing. SO: Project administration, Formal analysis, Supervision, Methodology, Writing – original draft, Funding acquisition, Writing – review & editing, Resources, Validation, Investigation, Visualization. AK: Resources, Funding acquisition, Investigation, Validation, Writing – review & editing, Project administration, Writing – original draft, Methodology, Visualization, Formal analysis, Supervision. WN: Writing – review & editing, Project administration, Investigation, Writing – original draft, Supervision, Funding acquisition, Visualization, Validation, Formal analysis, Resources, Methodology.

Funding

The author(s) declared that financial support was received for this work and/or its publication. RW was supported by the Deutsche Forschungsgemeinschaft (DFG, German Research Foundation, project number 513054523).

Acknowledgments

The authors thank Anna Störiko for providing support for model conceptualizations. AK thanks the support from the Deutsche Forschungsgemeinschaft (DFG, German Research Foundation) under Germany's Excellence Strategy - EXC 3121 - 533771652.

Conflict of interest

The author(s) declared that this work was conducted in the absence of any commercial or financial relationships that could be construed as a potential conflict of interest.

Generative AI statement

The author(s) declared that generative AI was used in the creation of this manuscript. Because none of the author(s) are native English speakers, generative AI tools were used for English-language editing, including grammar correction, sentence refinement, and improvements to clarity and readability. Generative AI was also used to assist with coding and figure visualization based on data compiled and interpreted by the author(s).

Any alternative text (alt text) provided alongside figures in this article has been generated by Frontiers with the support of artificial intelligence and reasonable efforts have been made to ensure accuracy, including review by the authors wherever possible. If you identify any issues, please contact us.

Publisher's note

Supplementary material

The Supplementary Material for this article can be found online at: https://www.frontiersin.org/articles/10.3389/frwa.2026.1844899/full#supplementary-material

References

Berg, M., Luzi, S., Trang, P. T. K., Viet, P. H., Giger, W., and Stüben, D. (2006). Arsenic removal from groundwater by household sand filters: comparative field study, model calculations, and health benefits. *Environ. Sci. Technol.* 40, 5567–5573. doi: 10.1021/es060144z

Boersma, A. S., Haukelidsaeter, S., Kirwan, L., Corbetta, A., Vos, L., Lenstra, W. K., et al. (2025). Influence of filter backwashing on iron, manganese, and ammonium removal in dual-media rapid sand filters used for drinking water production. *Water Res.* 270:122809. doi: 10.1016/j.watres.2024.122809

Chen, S., Dougherty, M., Chen, Z., Zuo, X., and He, J. (2021). Managing biofilm growth and clogging to promote sustainability in an intermittent sand filter (ISF). *Sci. Total Environ.* 755:142477. doi: 10.1016/j.scitotenv.2020.142477

Corbera–Rubio, F., Kruisdijk, E., Malheiro, S., Leblond, M., Verschoor, L., van Loosdrecht, M. C., et al. (2024). A difficult coexistence: Resolving the iron-induced nitrification delay in groundwater filters. *Water Res.* 260:121923. doi: 10.1016/j.watres.2024.121923

Dai, X. J., Xiao, X., Dai, W. T., Liu, S. H., Dong, X. Y., Shen, R. F., et al. (2023). Comparison of nitrate and ammonium leaching of soils collected from different regions of China: a soil column experiment. *J. Soil Sci. Plant Nutr.* 23, 6059–6070. doi: 10.1007/s42729-023-01464-4

Das, P., Penton, C. R., Bi, Y., and Westerhoff, P. (2023). Unraveling mechanisms behind reduced nitrate leaching with graphite nanomaterials addition with fertilizers in soil column experiments. *Chemosphere* 337:139417. doi: 10.1016/j.chemosphere.2023.139417

Dawi, M. A., Starnoni, M., Porta, G., and Sanchez-Vila, X. (2024). Pore-scale coupling of flow, biofilm growth, and nutrient transport: a microcontinuum approach. *Water Resour. Res.* 60:e2024WR038393. doi: 10.1029/2024WR038393

Di Curzio, D., Laureni, M., Broholm, M. M., Weissbrodt, D. G., and van Breukelen, B. M. (2024). Integrating enzyme-based kinetics in reactive transport models to simulate spatiotemporal dynamics of biomarkers during chlorinated ethene degradation. *Environ. Sci. Technol.* 58, 20642–20653. doi: 10.1021/acs.est.4c07445

Dou, Y., Howard, K. W., and Qian, H. (2016). Transport characteristics of nitrite in a shallow sedimentary aquifer in Northwest China as determined by a 12-day soil column experiment. *Expo. Heal.* 8, 381–387. doi: 10.1007/s12403-016-0206-x

European Union (2020). Directive (EU) 2020/2184 of the European Parliament and of the Council of 16 December 2020 on the quality of water intended for human consumption (recast). *Off. J. Eur. Union* L435, 1–62.

Gilani, B. I., and Prajapati, Y. N. (2024). Efficient adsorption of multi-heavy metal ions at trace-levels from groundwater using UiO-66 and activated carbon nanocomposites for safe drinking. *Ind. Eng. Chem. Res.* 63, 20327–20342. doi: 10.1021/acs.iecr.4c02399

Henze, M., Gujer, W., Mino, T., and van Loosedrecht, M. (2006). *Activated Sludge Models ASM1, ASM2, ASM2d and ASM3, Vol. 5.* London: IWA Publishing. doi: 10.2166/9781780402369

Hou, G., Wazir, Z. G., Liu, J., Wang, G., Rong, F., Xu, Y., et al. (2023). Effects of sulfadiazine and Cu on soil potential nitrification and ammonia-oxidizing archaea and bacteria communities across different soils. *Front. Microbiol.* 14:1153199. doi: 10.3389/fmicb.2023.1153199

Kruisdijk, E., van Breukelen, B. M., and van Halem, D. (2024). Simulation of rapid sand filters to understand and design sequential iron and manganese removal using reactive transport modelling. *Water Res.* 267:122517. doi: 10.1016/j.watres.2024.122517

Langergraber, G., and Šimůnek, J. (2005). Modeling variably saturated water flow and multicomponent reactive transport in constructed wetlands. *Vadose Zo. J.* 4, 924–938. doi: 10.2136/vzj2004.0166

Laurent, P., Andersson, A., Kihn, A., and Servais, P. (2003). Impact of backwashing on nitrification in the biological activated carbon filters used in drinking water treatment. *Environ. Technol.* 24, 277–287. doi: 10.1080/09593330309385560

Le, A. V., Muehe, E. M., Bone, S., Drabesch, S., Fischer, S., and Kappler, A. (2024). Field and laboratory evidence for manganese redox cycling controlling iron and arsenic retention in household sand filters. *ACS ES T Water* 4, 33–43. doi: 10.1021/acsestwater.3c00245

Le, A. V., Muehe, E. M., Drabesch, S., Lezama Pacheco, J., Bayer, T., Joshi, P., et al. (2022a). Environmental risk of arsenic mobilization from disposed sand filter materials. *Environ. Sci. Technol.* 56, 16822–16830. doi: 10.1021/acs.est.2c04915

Le, A. V., Straub, D., Planer-Friedrich, B., Hug, S. J., Kleindienst, S., and Kappler, A. (2022b). Microbial communities contribute to the elimination of As, Fe, Mn, and NH4+ from groundwater in household sand filters. *Sci. Total Environ.* 838:156496. doi: 10.1016/j.scitotenv.2022.156496

Liu, H., Maghoul, P., Shalaby, A., Bahari, A., and Moradi, F. (2020). Integrated approach for the MASW dispersion analysis using the spectral element technique and trust region reflective method. *Comput. Geotech.* 125:103689. doi: 10.1016/j.compgeo.2020.103689

Liu, Y. (2007). Overview of some theoretical approaches for derivation of the Monod equation. *Appl. Microbiol. Biotechnol.* 73, 1241–1250. doi: 10.1007/s00253-006-0717-7

Lundberg, S. M., and Lee, S. I. (2017). A unified approach to interpreting model predictions. *Adv. Neural Inf. Process. Syst.* 4766–4775. doi: 10.48550/arXiv.1705.07874

Maggi, F., and La Cecilia, D. (2016). Implicit analytic solution of Michaelis-Menten-Monod kinetics. *ACS Omega* 1, 894–898. doi: 10.1021/acsomega.6b00174

Malone, R. F., Bergeron, J., and Cristina, C. M. (2006). Linear versus Monod representation of ammonia oxidation rates in oligotrophic recirculating aquaculture systems. *Aquac. Eng.* 34, 214–223. doi: 10.1016/j.aquaeng.2005.08.005

Martikainen, K., Kauppinen, A., Matikka, V., Veijalainen, A. M., Torvinen, E., Pitkänen, T., et al. (2018). Efficiency of private household sand filters in removing nutrients and microbes fromwastewater in Finland. *Water* 10, 1–16. doi: 10.3390/w10081000

Nitzsche, K. S., Lan, V. M., Trang, P. T. K., Viet, P. H., Berg, M., Voegelin, A., et al. (2015). Arsenic removal from drinking water by a household sand filter in Vietnam-Effect of filter usage practices on arsenic removal efficiency and microbiological water quality. *Sci. Total Environ.* 502, 526–536. doi: 10.1016/j.scitotenv.2014.09.055

Niu, J., Kasuga, I., Kurisu, F., and Furumai, H. (2018). Effects of backwashing on granular activated carbon with ammonium removal potential in a full-scale drinking water purification plant. *Water* 10, 1–8. doi: 10.3390/w10121830

Noye, B. J., and Tan, H. H. (1989). Finite difference methods for solving the two-dimensional advection-diffusion equation. *Int. J. Numer. Methods Fluids* 9, 75–98. doi: 10.1002/fld.1650090107

Papirio, S., Zou, G., Ylinen, A., Di Capua, F., Pirozzi, F., and Puhakka, J. A. (2014). Effect of arsenic on nitrification of simulated mining water. *Bioresour. Technol.* 164, 149–154. doi: 10.1016/j.biortech.2014.04.072

Picetti, R., Deeney, M., Pastorino, S., Miller, M. R., Shah, A., Leon, D. A., et al. (2022). Nitrate and nitrite contamination in drinking water and cancer risk : a systematic review with meta-analysis. *Environ. Res.* 210:112988. doi: 10.1016/j.envres.2022.112988

Piñón-Villarreal, A. R., Bawazir, A. S., Shukla, M. K., and Hanson, A. T. (2013). Retention and transport of nitrate and ammonium in loamy sand amended with clinoptilolite zeolite. *J. Irrig. Drain. Eng.* 139, 755–765. doi: 10.1061/(ASCE)IR.1943-4774.0000618

Qu, C., Duan, C., Li, W., Wu, X., Liu, Z., Feng, F., et al. (2022). Understanding the slight inhibition of high As(III) stress on nitritation process: insights from arsenic speciation and microbial community analyses. *J. Hazard. Mater.* 435:128957. doi: 10.1016/j.jhazmat.2022.128957

Scheidegger, A. E. (1961). General theory of dispersion in porous media. *J. Geophys. Res.* 66, 3273–3278. doi: 10.1029/JZ066i010p03273

Schwarzenbach, R. P., Gschwend, P. M., and Imboden, D. M. (2005). *Environmental Organic Chemistry, 2nd Edn.* Hoboken, NJ: John Wiley & Sons Inc.

Shampine, L. F., and Reichelt, M. W. (1997). The MATLAB ODE suite. *SIAM J. Sci. Comput.* 18, 1–22. doi: 10.1137/S1064827594276424

Smith, A. C., Leng, M. J., McGowan, S., Panizzo, V. N., Ngo, T. T. T., Luu, T. N. M., et al. (2024). Identifying the controls on nitrate and metabolic state within the Red River delta (Vietnam) with the use of stable isotopes. *J. Hydrol.* 628:130467. doi: 10.1016/j.jhydrol.2023.130467

Sorwat, J., Mellage, A., Maisch, M., Kappler, A., Cirpka, O. A., and Byrne, J. M. (2021). Chromium (VI) removal kinetics by magnetite-coated sand: small-scale flow-through column experiments. *J. Hazard. Mater.* 415:125648. doi: 10.1016/j.jhazmat.2021.125648

Störiko, A., Pagel, H., Mellage, A., and Cirpka, O. A. (2021). Does it pay off to explicitly link functional gene expression to denitrification rates in reaction models? *Front. Microbiol.* 12:684146. doi: 10.3389/fmicb.2021.684146

Störiko, A., Pagel, H., Mellage, A., Van Cappellen, P., and Cirpka, O. A. (2022). Denitrification-driven transcription and enzyme production at the river-groundwater interface: Insights from reactive-transport modeling. *Earth Sp. Sci. Open Arch.* 58:e2021WR031584. doi: 10.1029/2021WR031584

Strobel, C., Abramov, S., Huisman, J. A., Cirpka, O. A., and Mellage, A. (2023). Spectral induced polarization (SIP) of denitrification-driven microbial activity in column experiments packed with calcareous aquifer sediments. *J. Geophys. Res. Biogeosci.* 128, 1–21. doi: 10.1029/2022JG007190

Tatari, K., Smets, B. F., and Albrechtsen, H. J. (2016). Depth investigation of rapid sand filters for drinking water production reveals strong stratification in nitrification biokinetic behavior. *Water Res.* 101, 402–410. doi: 10.1016/j.watres.2016.04.073

Truong, D. Q., Loganathan, P., Tran, L. M., Vu, D. L., Nguyen, T. V., Vigneswaran, S., et al. (2022). Removing ammonium from contaminated water using Purolite C100E: batch, column, and household filter studies. *Environ. Sci. Pollut. Res.* 29, 16959–16972. doi: 10.1007/s11356-021-16945-1

Vu, C. T., and Wu, T. (2022). Enhanced slow sand filtration for the removal of micropollutants from groundwater. *Sci. Total Environ.* 809:152161. doi: 10.1016/j.scitotenv.2021.152161

Winkel, L. H., Trang, P. T. K., Lan, V. M., Stengel, C., Amini, M., Ha, N. T., et al. (2011). Arsenic pollution of groundwater in Vietnam exacerbated by deep aquifer exploitation for more than a century. *Proc. Natl. Acad. Sci. U. S. A.* 108, 1246–1251. doi: 10.1073/pnas.1011915108

World Health Organization (2016). *Nitrate and Nitrite in Drinking-Water: Background Document for Development of Who Guidelines for Drinking-Water Quality*. Technical Report. Geneva: World Health Organization.

Wu, Z., Dougherty, M., Chen, Z., Zhou, Y., Zuo, X., and He, J. (2022). Interaction between bioaccumulation and the efficiency of intermittent sand filters in wastewater treatment. *J. Clean. Prod.* 335:130303. doi: 10.1016/j.jclepro.2021.130303

Yang, X., Wan, Y., Zheng, Y., He, F., Yu, Z., Huang, J., et al. (2019). Surface functional groups of carbon-based adsorbents and their roles in the removal of heavy metals from aqueous solutions: a critical review. *Chem. Eng. J.* 366, 608–621. doi: 10.1016/j.cej.2019.02.119